Editors' Suggestion

Three-dimensional niobium coaxial cavity with 0.1-second lifetime

Takaaki Takenaka,[1,*,†] Takayuki Kubo,[2,3,†] Imran Mahboob,[1] Kosuke Mizuno,[1,‡] Hitoshi Inoue,[2] Takayuki Saeki,[2,3] and Shiro Saito[1]

[1] *Basic Research Laboratories, NTT, Inc., 3-1 Morinosato-Wakamiya, Atsugi, Kanagawa 243-0198, Japan*
[2] *High Energy Accelerator Research Organization (KEK), Tsukuba, Ibaraki 305-0801, Japan*
[3] *The Graduate University for Advanced Studies (Sokendai), Hayama, Kanagawa 240-0193, Japan*

(Received 20 October 2025; revised 19 January 2026; accepted 4 February 2026; published 24 March 2026)

We report on the internal quality factor of a three-dimensional niobium quarter-wave coaxial cavity that has undergone mid-temperature annealing, exhibiting $Q_{\rm int} \gtrsim 3 \times 10^9$ at the single-photon level below 20 mK, which corresponds to an internal photon lifetime of $\tau_{\rm int} \sim 90$ ms. Moreover, $Q_{\rm int}$ of the mid-temperature-annealed cavities remains almost unchanged even after several cooldown cycles and air exposure. These results suggest that stable low-loss niobium oxides are formed by mid-temperature annealing on the surface of a three-dimensional niobium cavity. This surface treatment could be applicable to the fabrication of two-dimensional superconducting circuits and help improve the lifetime of Nb-based superconducting qubits.

DOI: 10.1103/5nf2-tjb9

I. INTRODUCTION

Three-dimensional (3D) superconducting cavities with high internal quality factor ($Q_{\rm int}$) are gaining attention for quantum information processing and sensing. The well-controlled electromagnetic environment of a 3D cavity enables the realization of a 3D circuit quantum electrodynamics (cQED) architecture with desired coupling between the superconducting qubit and the cavity while maintaining the long lifetime of the cavity [1,2]. This architecture is a promising platform for quantum information processing using the large Hilbert space of the resonator [3–6]. Recently, high-Q 3D cavities have also been used to measure dielectric losses of the substrates for superconducting qubits [7,8] and in the search for dark photon dark matter [9–11].

High-purity aluminum is widely used in 3D cQED architectures due to its ease of machining and commercial availability, with internal quality factors $Q_{\rm int}$ reaching approximately 1×10^8 [2,12]. Niobium is extensively employed in superconducting radio-frequency (SRF) cavities for particle accelerators, where internal quality factors exceeding 1×10^{11} have been demonstrated [13–15], which motivates us to apply SRF-based knowledge to cQED devices; however, SRF cavities operate under extremely high radio-frequency (rf) fields, typically with electric fields $E > \mathcal{O}(10)$ MV/m at 1.4 K [16–18]. For this reason, surface treatments have been specifically developed to mitigate issues arising under such intense electromagnetic conditions [19], including electron field emission [20,21], degradation of Q due to hydrogen contamination near the surface [22] (commonly referred to as Q disease [23,24]), rf-induced breakdown of superconductivity [25,26], and magnetic flux trapping during cooldown [27,28]. In contrast, cQED devices operate at millikelvin temperatures with low numbers of photons ($\bar{n} < 10^4$), where losses due to two-level systems (TLSs) become one of the limiting mechanisms for $Q_{\rm int}$. Therefore, surface treatments developed for niobium SRF cavities cannot be directly translated to cQED devices, and alternative surface treatments are necessary.

Recent studies have reported that $Q_{\rm int}$ at low electric fields can exceed 10^9 by optimizing the cavity geometry [29,30] or by applying water-buffered oxide etching at temperatures below 10 °C to remove residual fluorine [31]; however, $Q_{\rm int}$ tends to degrade after air exposure or repeated thermal cycling, likely due to the growth of native oxides or NbH_x formation from surface hydrogen. Vacuum storage [15,32] and rapid cooldown protocols to suppress hydrogen migration [23] can mitigate these

*Contact author: takaaki.takenaka@ntt.com
†These authors contributed equally to this work.
‡Present address: Global Research and Development Center for Business by Quantum-AI Technology (G-QuAT), National Institute of Advanced Industrial Science and Technology (AIST), Tsukuba, Ibaraki 305-8568, Japan.

effects, but such procedures are often incompatible with the operational constraints of quantum devices and their measurement environments. In contrast, annealing niobium under vacuum is simple and yields various improvements in SRF cavities; annealing at temperatures above 700 °C can effectively remove hydrogen from the surface [24], and additional mid-temperature annealing has achieved a remarkably low surface resistance of 0.2 nΩ [33]. Therefore, vacuum annealing of niobium could ensure a stable and high-quality surface even under low-microwave-field conditions, which is crucial for realizing the full potential of niobium in quantum applications.

In this paper, we investigate optimal surface-treatment procedures for niobium cavities to achieve high Q_{int} at millikelvin temperatures and low electromagnetic fields. Specifically, we explore the appropriate sequence and combination of surface-treatment techniques developed in the SRF community, such as heat treatments at various temperatures. For instance, high-temperature baking at 900 °C after buffered chemical polishing (BCP) can improve Q_{int}, although this procedure is not sufficient to prevent degradation over multiple cooldown cycles. In contrast, after subsequent mid-temperature annealing, inspired by Ref. [33], we find Q_{int} reaching approximately 3.0×10^9 at the single-photon level, twice the highest Q_{int} of approximately 1.5×10^9 previously reported for coaxial cavities. This performance remains nearly unchanged even after several cooldown cycles with 10 h of air exposure. These results are consistent with a reduced fraction of Nb_2O_5 on the surface, as revealed by x-ray photoelectron spectroscopy (XPS) measurements. Notably, this treatment process does not require SRF-specific procedures such as electropolishing or high-pressure rinsing, and it is compatible with Nb-based superconducting qubit fabrication processes.

II. METHODS

Quarter-wave coaxial stub cavities [Figs. 1(a) and 1(b)] are machined from a block of high-conductivity Nb with a residual resistivity ratio (RRR) of ≥300 that was procured from Tokyo Denkai Co., Ltd. The height of the center stub is $h = 12.0$ mm, which yields a $\lambda/4$ mode with resonance frequency $f_r \sim 5.5$ GHz. The radii of the outer wall and the center post are $r_{\text{out}} = 5.4$ mm and $r_{\text{in}} = 2.0$ mm, respectively; these dimensions are chosen to minimize the conductor losses of the $\lambda/4$ mode after 100–150 μm of surface etching. The center stub was fabricated in two ways: either by machining alone (A series) or by machining followed by finishing with electrical discharge machining (EDM; B series). We fabricated cavities using different machining methods because surface roughness can influence Q_{int}; however, after applying these surface treatments, no substantial difference in Q_{int} was observed between them.

The cavities were first tested in their as-machined condition (no additional surface treatment), and they were subsequently subjected to a series of surface treatments at the

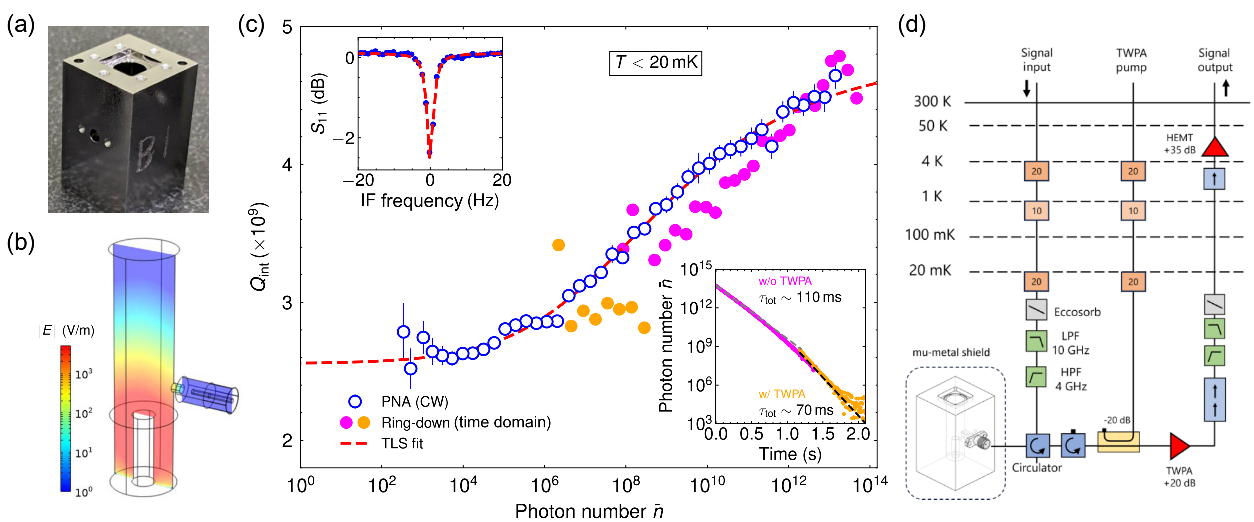

FIG. 1. (a) Photograph of the niobium cavity used in this study. (b) Simulated electric field distribution for the $\lambda/4$ mode of the coaxial cavity with input voltage $V_{\text{in}} = 0.1$ V from the external coupling port. (c) Characterization of the internal quality factor Q_{int} of cavity B2 after a mid-temperature anneal for 3 h at 600 °C. The internal quality factor as a function of the average photon number $\bar{n}$ in the cavity is fitted using the standard TLS model [Eq. (1)] and is shown by the red dashed line with $F\delta^0_{\text{TLS}} = 1.82 \times 10^{-10}$, $n_c = 2.0 \times 10^6$, $\beta = 0.34$, and $Q_{\text{res}} = 4.77 \times 10^9$. Here, Q_{int} (points) is extracted from both S_{11} reflection spectra (upper inset) and ring-down measurements (lower inset). Ring-down measurements are performed both with (orange) and without (magenta) a traveling-wave parametric amplifier (TWPA) since the quantum-limited amplifier saturates under a high-power signal. Note that these data were obtained in the second cooldown, after exposing the cavity to air for 10 h, leading to an insignificant degradation of Q_{int} compared to the first cooldown. (d) Schematic of the low-temperature part of the measurement setup employed for this experiment.

Cavity Fabrication Facility [34] of the High Energy Accelerator Research Organization. Our approach followed the fundamental steps of standard procedures established for superconducting cavities used in particle accelerators, with high-field-specific preparations being deliberately omitted. The simplified version of the SRF surface treatment protocol used in this study is as follows.

(1) Removal of approximately 100 μm of material from the inner surface using BCP at room temperature ($\gtrsim 20^{\circ}$C).
(2) Baking the cavity in a vacuum furnace at 900 °C for 3 h (high-T bake).
(3) Light BCP ("BCP flush") to remove a few additional micrometers of material.
(4) Additional treatment for surface optimization.

The meaning and purpose of each step are briefly reviewed in Appendix A, and the estimation of removal depth by BCP is described in Appendix B. In step 4, which is a purpose-specific step, various treatment options exist in SRF protocols, ranging from those optimized for high accelerating fields to those aimed at minimizing surface resistance for high-Q performance. Reference [33] suggests that a mid-temperature anneal at $T \simeq 600\,^{\circ}$C significantly reduces the residual surface resistance. In Ref. [35], similar results were recently reported in low fields where losses arising from TLSs are finite; therefore, mid-temperature annealing might be effective for quantum applications. We examine and compare the following three options for this step: (4a) no additional treatment, (4b) annealing at 460 °C for 3 h, and (4c) annealing at 600 °C for 3 h.

After completing the surface treatment, the cavities were set for a reflection geometry (S_{11}) and mounted in a dilution refrigerator at a base temperature below 20 mK. Cavity performance was evaluated using both frequency-domain and time-domain measurements. For the frequency-domain measurements, we used a standard vector network analyzer (VNA) with an intermediate frequency (IF) bandwidth of 1 Hz. The time-domain measurements were carried out with Quantum Machines' OPX+ and Octave system. The experimental cryogenic setup employed in this study is shown in Fig. 1(d).

III. Q_{int} AT BASE TEMPERATURES

Figure 1(c) summarizes the dependence of Q_{int} on the average photon number $\bar{n}$ for cavity B2, following 100 μm BCP, 900 °C baking for 3 h, BCP flush, 600 °C annealing for 3 h, and 10 h of air exposure. The upper inset of Fig. 1(c) displays the magnitude of the reflection coefficient S_{11}. The experimental data are reproduced by a circle fit (dashed line), from which $Q_{\mathrm{int}} \sim 3.0 \times 10^9$ and $Q_{\mathrm{ext}} \sim 17 \times 10^9$ are extracted [36]. The lower inset of Fig. 1(c) shows the ring-down measurement, yielding the total cavity decay time of approximately 110 ms in the high-photon regime (magenta) and 70 ms at low photon numbers (orange). The internal decay time can then be extracted using $\tau_{\mathrm{tot}}^{-1} = \tau_{\mathrm{ext}}^{-1} + \tau_{\mathrm{int}}^{-1}$ and $\tau_{\mathrm{ext}} = Q_{\mathrm{ext}}/(2\pi f_r)$, resulting in $\tau_{\mathrm{int,high}} \sim 141$ ms and $\tau_{\mathrm{int,low}} \sim 80$ ms, respectively. The two datasets show agreement across a wide range of photon numbers, demonstrating the reliability and reproducibility of both measurement results.

The average photon-number dependence of Q_{int} in the low-temperature regime $T < 1.2$ K is described by the standard TLS model [15,37–42]

$$\frac{1}{Q_{\mathrm{int}}(\bar{n})} = F\delta^0_{\mathrm{TLS}} \frac{\tanh\left(\frac{hf_r}{2k_BT}\right)}{\sqrt{1+\left(\frac{\bar{n}}{n_c}\right)^{\beta}}} + \frac{1}{Q_{\mathrm{res}}}, \tag{1}$$

where $F = t_{\mathrm{ox}} \int_S |E^2|\, dS / \int_V \epsilon_r |E^2|\, dV$ is the geometric factor of the TLSs, δ^0_{TLS} is the loss tangent of the oxide layer with $T \to 0$ at the single-photon level (effectively proportional to the TLS density), k_B is the Boltzmann constant, n_c is the critical photon number for TLS saturation, β is a fitting parameter that reflects the geometry of the cavity, and Q_{res} is the residual quality factor that arises from magnetic defects or other non-TLS-related losses [27,28,43,44]. We simulate the surface electric participation ratio $S_e = \int_S |E|^2\, dS / \int_V |E|^2\, dV \sim 650$ using COMSOL MULTIPHYSICS and obtain $F \sim 1.07 \times 10^{-7}$, assuming the thickness and relative permittivity of the niobium oxide layer are $t_{\mathrm{ox}} = 5$ nm and $\epsilon_r = 30$ [35], respectively. The red dashed line in Fig. 1(c) represents the fit from Eq. (1), indicating that Q_{int} is limited by TLS losses for photon numbers below $n_c \sim 10^6$, and it approaches the value at single-photon level, approximately 3×10^9 [Fig. 1(c)].

IV. TEMPERATURE DEPENDENCE OF Q_{int}

The evolution of $Q_{\mathrm{int}}(T)$ after each treatment process is shown in Fig. 2 and Appendix F. Without surface treatment, Q_{int} is less than 1×10^8 for all cavities. The cavity fabricated by machining (cavity A2) exhibits an order-of-magnitude higher Q_{int} than that fabricated by EDM (cavity B2), and their temperature dependence differs significantly (blue symbols in Fig. 8). This behavior most likely originates from the formation of a low-$T_c \sim 1$ K material on the cavity surface from EDM.

After high-temperature baking and subsequent BCP flush, all cavities reach $Q_{\mathrm{int}} \sim 1 \times 10^9$ at base temperature ($T < 20$ mK) and exhibit a peak around $T \sim 1.2$ K (green symbols in Fig. 2). The temperature dependence of Q_{int} with low input power ($\bar{n} \sim 1 \times 10^4$) is fitted by the

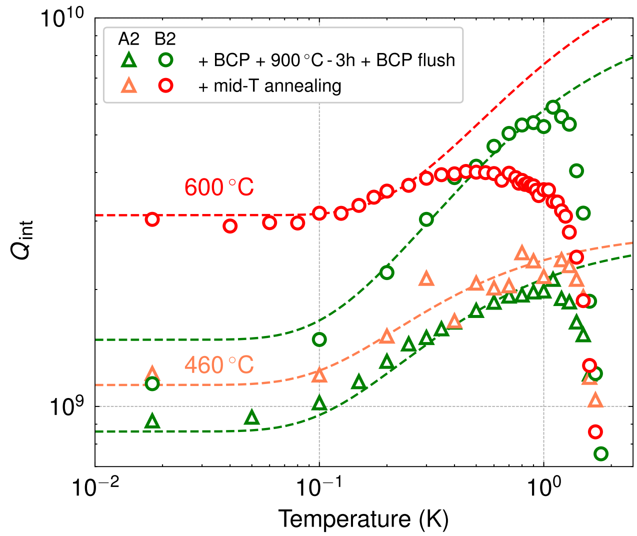

FIG. 2. Temperature dependence of the internal quality factor $Q_{\rm int}$ after each surface treatment. The dashed lines are fits to the temperature-dependent TLS model [Eq. (2)] using low-power data. Results are shown for cavities A2 and B2 after 100 μm BCP + 900 °C for 3 h + BCP flush (green), and subsequent mid-temperature annealing at 460 °C or 600 °C for 3 h (red and orange). These measurements were performed at an average photon number of $\bar{n} \sim 10^4$.

temperature-dependent TLS model [15,31,41]

$$\frac{1}{Q_{\rm int}(T)} = F\delta^0_{\rm TLS} \tanh\left(\frac{hf_r}{2k_BT}\right) + \frac{1}{Q_{\rm int,0}}. \quad (2)$$

Curves of $Q_{\rm int}(T)$ below 1.0 K are well reproduced using the same $F\delta^0_{\rm TLS}$ obtained from the power-dependent TLS model [Eq. (1)], typically 0.5–1.0 $\times$ 10^{-9} (see Appendix F for details), thus indicating that the same TLSs govern the low-temperature behavior.

Subsequent annealing at 460 °C for 3 h improves $Q_{\rm int}$ by a factor of 1.5, whereas 600 °C annealing leads to a further improvement by a factor of 3 (red and orange symbols in Fig. 2). We find that $F\delta^0_{\rm TLS}$ is also reduced by the mid-temperature annealing, with values of approximately 4.9×10^{-10} for 460 °C annealing and approximately 2.1×10^{-10} for 600 °C annealing. The difference between the 460 and 600 °C annealing is also reflected in the temperature dependence of $Q_{\rm int}$. The 460 °C-annealed cavity exhibits a peak in $Q_{\rm int}$ around 1.2 K, similar to the cavities without mid-temperature annealing as well as SRF cavities [15]. In contrast, the 600 °C-annealed cavity shows its maximum $Q_{\rm int}$ around 0.3 K, a behavior previously reported only in water-buffered chemically etched cavities [31]. This difference will be discussed later.

The low-TLS-loss property of the niobium cavity surface after mid-temperature annealing can also be confirmed through observations of resonance frequency shifts as a function of temperature. At low temperatures, TLS-induced resonance frequency shifts can be described by the following expression [40,42,45]:

$$\frac{\delta f}{f_r} = \frac{F\delta^0_{\rm TLS}}{\pi}\left[{\rm Re}\Psi\left(\frac{1}{2} + \frac{1}{2\pi i}\frac{hf_r}{k_BT}\right) - \log\left(\frac{hf_r}{2\pi k_BT}\right)\right], \quad (3)$$

where ReΨ denotes the real part of the complex digamma function. Equation (3) gives a frequency minimum around $T \sim hf_r/k_B$, which corresponds to about 120 mK in our 5.5-GHz cavities. Figure 3 shows the evolution of the normalized frequency shift $\delta f/f_r$ and $Q_{\rm int}$ for cavity B2 with cooldown cycles and air exposures. Before mid-temperature annealing, a clear frequency shift from base temperature to 120–200 mK indicates the presence of a non-negligible density of TLSs in the oxide layer on the cavity surface. In the second cooldown, the frequency shift becomes more pronounced, and $Q_{\rm int}$ decreases to approximately one-fifth of that in the first cooldown, suggesting an increase in $F\delta^0_{\rm TLS}$ and the associated rise in total loss originating from the change in the TLS density. In contrast, after 600 °C mid-temperature annealing, the frequency shift is dramatically suppressed when $T < 1.0$ K, in conjunction with an increased $Q_{\rm int}$, thus indicating a reduction in TLS density.

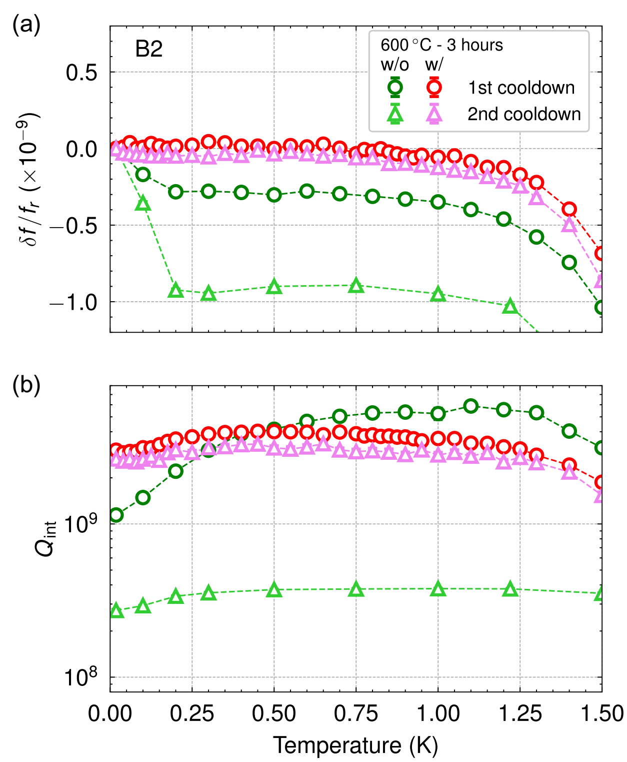

FIG. 3. Temperature dependence of the (a) normalized frequency shift $\delta f/f_r$ and (b) internal quality factor $Q_{\rm int}$ for cavity B2 measured across multiple cooldown cycles, before and after 600 °C mid-temperature annealing.

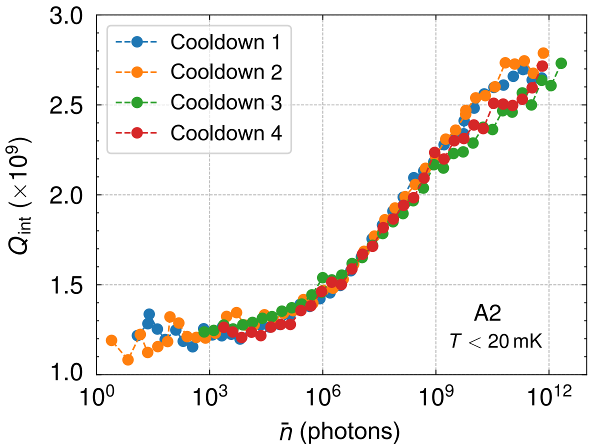

FIG. 4. Comparison of Q_{int} as a function of the average photon number $\bar{n}$ in cavity A2 after 460 °C annealing over multiple cooldown cycles. The cavity was exposed to air for approximately 2 h between each cooldown cycle, which confirms the stability of the cavity performance against air exposure. The Q_{int} value is extracted from S_{11} spectral measurements with the VNA.

Remarkably, this improved behavior remains nearly unchanged even after 10 h of air exposure followed by a cooldown, suggesting that the TLS density has not only been significantly reduced but it has also been stabilized by the 600 °C mid-temperature annealing process. The 460 °C-annealed cavity A2 also maintains a high Q value over multiple cooldown cycles, and its power dependence remains unchanged, as shown in Fig. 4. In typical niobium cavities for quantum applications that only undergo bulk BCP, Q_{int} drops after several cooldown cycles, and the resultant temperature dependence indicates the occurrence of hydrogen Q disease [29,31]. Indeed, our 900 °C-baked cavities also show similar degradation in Q_{int} within a few cooldown cycles. This contrasting behavior suggests that mid-temperature annealing plays a significant role in stabilizing the niobium cavities against air exposure and repeated cooldown cycles.

V. DISCUSSION

After 900 °C baking for 3 h followed by a BCP flush, our cavities exhibited a 2–3-fold improvement in Q_{int} compared to previous coaxial cavities treated with conventional BCP alone [31,45]. The key difference between our method and previous studies lies in the duration of niobium surface exposure to the BCP solution. Previously, BCP was typically performed for approximately 2 h, and such prolonged exposure to conventional BCP solutions is reported to result in fluoride residue near the surface [31] and to promote hydrogen absorption. In contrast, our method also begins with an initial 100-μm bulk BCP, followed by 900 °C baking, which causes contaminants to precipitate onto the surface. A subsequent short-duration BCP flush then effectively removes these impurities and residues. Note that fluoride formation should be minimal because the BCP flush lasts only about 30 s (see Appendix B for details). XPS measurements (Appendix E) reveal that a small amount of fluorine remains on the niobium surface after the initial 100-μm bulk BCP, which disappears following high-temperature annealing and BCP flush. This result is consistent with the findings of Oriani *et al.* [31], who demonstrated that H_2O-buffered etching provides better performance than conventional H_3PO_4-buffered etching due to the elimination of fluoride residue on cavity surface.

The further improvement in Q_{int} observed after mid-temperature annealing is attributed to modifications to the surface oxides. It is well established that vacuum annealing at temperatures above 340 °C dissolves Nb_2O_5, which also leads to a reduction in the loss tangent δ^0_{TLS} in SRF cavities [46–48]. The correlation between the amount of Nb_2O_5 and the quality factor was also demonstrated in two-dimensional superconducting circuits at low temperatures of approximately 10 mK, both by controlling the thickness of the Nb_2O_5 layer [49] and by selectively removing Nb_2O_5 from the surface [42]. Figure 5 shows a high-resolution scan of the Nb 3d region before and after 600 °C annealing. Before applying 600 °C annealing, clear peaks corresponding to Nb_2O_5 are observed around 210 eV, while after annealing, those peaks are reduced and NbO-related peaks around 204 eV become more pronounced. The composition ratio of Nb_2O_5 decreases from approximately 60% to 40%, while NbO increases from approximately 10% to 40% (see Appendix E for details). These findings are consistent with the recent study by

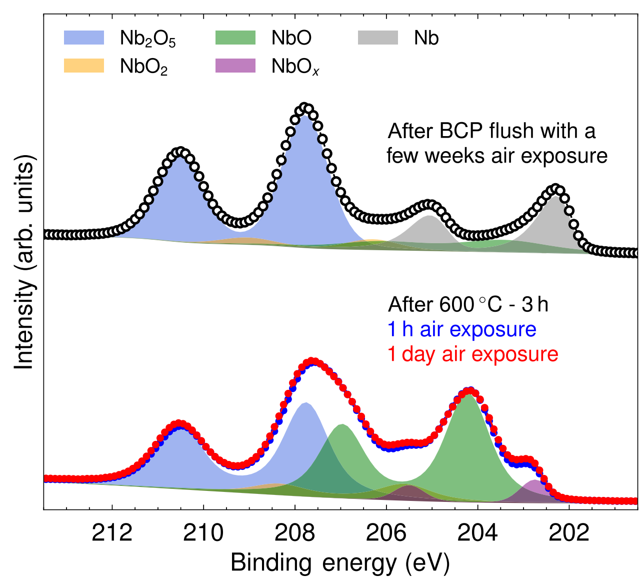

FIG. 5. XPS spectra of the Nb 3d region after a BCP flush and subsequent 600 °C annealing with post-anneal air exposures of 1 h and 1 day. Peaks corresponding to Nb_2O_5, NbO_2, NbO, NbO_x ($0 < x < 1$), and metallic Nb are indicated with filled areas.

Kalboussi *et al.* [35], which demonstrated that 650 °C vacuum annealing increased Q_{int} by approximately an order of magnitude at $T \sim 1.4$ K.

This modification of the surface niobium oxides is consistent with the distinct temperature dependence of Q_{int} observed in the 600 °C-annealed cavity, as shown in Fig. 2. At low temperatures, the behavior of $Q_{\mathrm{int}}(T)$ can be attributed to the interplay between TLS losses and quasiparticle excitations, with the latter typically becoming significant when $T/T_c \gtrsim 0.3$, which corresponds to $T \simeq 0.4$ K for NbO with $T_c \sim 1.4$ K. The experimental observation that Q_{int} reaches a maximum at $T \sim 0.3$ K after 600 °C annealing, together with the emergence of a frequency shift at $T \gtrsim 0.5$ K, is therefore consistent with the temperature scale at which quasiparticle excitations in NbO become non-negligible.

The substantial presence of NbO near the surface could account for the stability of Q_{int} against air exposure. It has been suggested that on an unannealed niobium surface, the Nb_2O_5 layer grows over time, whereas NbO_2 and NbO remain at monolayer thickness [49]. In contrast, it has been reported that 300–600°C annealing increases the thickness of the NbO layer between Nb_2O_5 and metallic Nb [35,48], which can slow oxide growth by increasing the potential barrier for oxygen incorporation. Our observation—that Q_{int} remains stable under air exposure or thermal cycles after annealing at 460 °C or 600 °C—is consistent with these studies. The presence of a thick NbO layer on the Nb surface might be harmful to SRF applications in which cavities operate at $T \sim 1.4$ K. For quantum applications, however, such a layer is unlikely to degrade performance because the devices operate well below the T_c of NbO; moreover, it helps stabilize performance under repeated operations. Therefore, although mid-temperature annealing in vacuum is much simpler than the sophisticated techniques used for SRF cavities, it has the potential to be a more practical approach to achieving improved performance in Nb-based quantum devices.

VI. CONCLUSIONS

In summary, we have demonstrated that an SRF-inspired surface treatment recipe significantly improves the internal quality factor Q_{int} of niobium coaxial cavities at low temperatures of approximately 20 mK and at the single-photon level. After applying 100-μm BCP, 900 °C baking for 3 h, and subsequent BCP flush for outermost surface removal, all cavities exhibit $Q_{\mathrm{int}} \sim 1 \times 10^9$. The value of Q_{int} is then further improved by an additional 600 °C annealing for 3 h, achieving a record-breaking value of $Q_{\mathrm{int}} \sim 3 \times 10^9$ in $\lambda/4$ coaxial cavities. Moreover, no significant degradation is observed in Q_{int} with repeated cooldown cycles or air exposure, which has been a major issue in niobium cavities for quantum applications. Experimental observations indicate that these improvements are associated with a reduced fraction of Nb_2O_5, while NbO increases due to mid-temperature annealing. Our findings suggest that the long-standing knowledge from SRF cavity research is also beneficial for quantum applications, and it could potentially enable the realization of long-lived Nb-based superconducting quantum devices.

ACKNOWLEDGMENTS

The authors thank T. Nitta for fruitful discussions. We also acknowledge T. Matsushima for his work on XPS measurements, and K. Kakuyanagi and H. Toida for technical assistance. The cavities were manufactured by Ono-Denki Co. and Top Seiko Co., Ltd. This work was supported by JST Moonshot R&D, Grant No. JPMJMS2067. The work of T.K. was supported by JSPS KAKENHI Grant No. JP25K23386.

DATA AVAILABILITY

The data that support the findings of this article are not publicly available upon publication because it is not technically feasible and/or the cost of preparing, depositing, and hosting the data would be prohibitive within the terms of this research project. The data are available from the authors upon reasonable request.

APPENDIX A: SURFACE TREATMENT

Step 1 is the bulk BCP, which plays a critical role in removing the damaged surface layer introduced during fabrication. Decades-old experiments [50] have shown that cavities with minimal surface removal exhibit surface resistance nearly an order of magnitude higher than those with approximately 100 μm of material removed. The chemical solution used for surface removal consists of hydrofluoric acid (HF, 46%), nitric acid (HNO_3, 60%), and phosphoric acid (H_3PO_4, 85%) mixed in a 1 : 1 : 1 volume ratio. The surface-removal process is governed by the following chemical reactions: $6\,Nb + 10\,HNO_3 \rightarrow 3\,Nb_2O_5 + 10\,NO + 5\,H_2O$ and $Nb_2O_5 + 10\,HF \rightarrow 2\,NbF_5 + 5\,H_2O$. In this process, nitric acid first oxidizes the niobium surface to form a niobium pentoxide layer, which is subsequently dissolved by hydrofluoric acid. Although phosphoric acid does not directly participate in the chemical reactions, it serves to increase the viscosity of the solution and to moderate the overall reaction rate. Under the standard 1 : 1 : 1 mixture at room temperature (approximately 25 °C), the etching rate is typically around 10 μm/min. Increasing the proportion of phosphoric acid is known to slow the etching rate and to produce a smoother surface; a 1 : 1 : 2 volume ratio is sometimes employed in SRF cavity processing for this reason; however, the impact of surface roughness on the Q factor in the quantum regime remains unclear.

Therefore, in this study, we adopt the standard 1 : 1 : 1 volume ratio BCP process at room temperature. In this study, we achieved an internal quality factor of $Q_{\text{int}} \geq 1.0 \times 10^9$ through a combination of the following procedures. These results suggest that achieving high Q_{int} in the low-power regime does not depend critically on the etching rate, and that room-temperature BCP is sufficient. After BCP, the cavities were rinsed and ultrasonically cleaned in ultrapure water for 15 min.

Step 2 is also a well-established process following BCP or electropolishing [51]. Annealing at temperatures above around 700 °C is essential to degas hydrogen and to prevent the onset of so-called "hydrogen Q disease," a form of Q degradation first identified in the late 1980s [23,24]. Hydrogen Q disease occurs when hydrogen introduced during BCP or electropolishing remains in the niobium lattice as a solid solution at room temperature. Upon cooling to around 100 K, this hydrogen precipitates as niobium hydride. Niobium hydride, which has a superconducting transition temperature of $T_c \sim 1$ K, exhibits significantly higher surface resistance than pure niobium, thereby degrading the Q value. This degradation can be avoided by rapidly cooling the cavity through the temperature region near 100 K [23,24]. Alternatively, hydrogen can be effectively removed by vacuum annealing at temperatures above 700 °C, which significantly reduces the risk of hydride formation [24]. This issue becomes more pronounced in higher-purity niobium. Modern commercially available niobium often exhibits residual resistivity ratio values exceeding 300, making proper hydrogen degassing treatment even more critical for avoiding hydrogen Q disease.

Another important aspect of annealing is its role in mitigating flux pinning. It is well established that environmental magnetic flux, such as geomagnetic fields or the magnetization of metal components, can become trapped during the cooldown of a cavity, increasing surface resistance and limiting the Q factor, recognized over half a century ago (e.g., Ref. [52]). Empirically, annealing at temperatures $\gtrsim$900 °C has been shown to significantly reduce the amount of trapped flux, leading to improved Q factors [53]. Furthermore, dynamic studies of vortex behavior in cavity-grade niobium have demonstrated substantially different behavior in annealed niobium [54,55].

Step 3 is the BCP flush, which is intended to remove surface contamination introduced during the annealing process. Extensive experience across the SRF community indicates that cavity performance is sensitive to the cleanliness of the vacuum furnace, particularly when a light BCP or electropolishing step after annealing is omitted [56,57]. In many SRF processing protocols, light electropolishing of a few micrometers is commonly applied after annealing. Electropolishing [51] also provides a smoother surface than BCP; therefore, it is the standard process in modern SRF cavity fabrication. Since the impact of surface roughness on the quality factor Q in the quantum regime remains unclear, we instead employ a BCP flush, which is also used in modern large-scale accelerator projects [58]. After the BCP flush, the cavities were rinsed and ultrasonically cleaned in ultrapure water for 15 min. In cavity A1 and B1, the BCP flush was repeated twice and the Q_{int} value improved after the second BCP flush (see Appendix F).

Step 4 is a purpose-specific step. For high-field SRF cavities, a low-temperature vacuum anneal at approximately 100 °C for 48 h [59] or its modified version [60] is typically employed at this stage. The low-temperature vacuum bake is known to diffuse oxygen localized near the surface into the bulk [61,62], thereby modifying the mean-free-path distribution within the London penetration depth. This redistribution is theoretically expected to suppress the surface screening current and enhance the quench field [63–65]. When moderately high fields are required in combination with high Q values, as in certain accelerator applications, a mid-temperature annealing [32,33,66] is often employed instead. For SRF cavities operating at 2 K, where the thermally excited quasiparticle contribution is the dominant factor limiting the Q value [43,44,67], the optimum mid-T bake temperature is considered to lie in the range 300–400 °C; however, in our quantum application, the optimum mid-T annealing temperature did not necessarily coincide with this range. Moreover, Ref. [33] suggests that a mid-temperature annealing at approximately $T \gtrsim 600$ °C significantly reduces the residual surface resistance and may be effective for quantum applications. A more recent study [35], published during the course of our project, also reports the effectiveness of annealing at a similar temperature.

Note that in SRF applications, high-pressure water rinsing [68,69] and subsequent clean-room assembly—both essential to suppress field emission under high-field operation—are normally performed, but they were omitted in this study.

APPENDIX B: ESTIMATION OF MATERIAL-REMOVAL DEPTH

Here, we describe the procedure used to estimate the amount of material removed during chemical polishing, Δt. At KEK, two independent methods are employed in parallel, and their results are compared to ensure consistency:

(1) **Direct measurement using a thickness gauge.** The cavity-wall thickness is measured before and after BCP using a mechanical gauge at predefined reference points.

(2) **Indirect measurement based on weight loss.** The cavity is weighed before and after BCP using a precision balance, and the removed thickness is estimated assuming

uniform etching as $\Delta t = \Delta w/(\rho S)$, where Δw is the mass loss, $\rho = 8.57$ g/cm^3 is the material density of niobium, and S is the surface area (110.591 cm^2 for cavities A1 and A2 and 107.98 cm^2 for cavities B1 and B2).

The bulk BCP (Step 1) was conducted at 20 °C for 12 min. The amount of material removed was estimated as follows. Using a thickness gauge, the measured removal depths were 112, 100, 104, and 94 μm for cavities A1, A2, B1, and B2, respectively. In contrast, the corresponding weight losses were $\Delta w = 9.54, 9.46, 8.90$, and 8.98 g, which translate to estimated removal depths of $\Delta t = 101$, 100, 96, and 97 μm for A1, A2, B1, and B2, respectively, assuming uniform etching and known material density. These results confirm that approximately 100 μm of material was successfully removed from each cavity.

The BCP flush (Step 3) was conducted at 20 °C for 30 s. The amount of material removed was estimated solely by weight loss, since the removal depth was too small to be measured directly using a thickness gauge. The measured weight losses were $\Delta w = 0.41$ and 0.39 g, which correspond to estimated removal depths of $\Delta t = 4.3$ and 4.2 μm for A2 and B2, respectively.

APPENDIX C: H_2O BCP FLUSH

We tested a modified BCP solution based on the formulation adopted in Ref. [31], in which water is used as the buffering component instead of H_3PO_4 in the standard BCP mixture. We refer to this solution as wBCP in what follows.

In the first trial, a 1 : 1 : 1 volume ratio of HF, HNO_3, and ultrapure water was used at room temperature. Before mixing, the room temperature, which also determines the initial temperature of each chemical, was approximately 16 °C. Upon mixing HNO_3 and water, however, the solution temperature rapidly increased to 36 °C. After subsequently adding room-temperature HF and waiting for several minutes, the wBCP solution stabilized at approximately 23 °C. A wBCP flush was then applied to the A1 and B1 cavities for 25 s, followed by rinsing and ultrasonic cleaning in ultrapure water for 15 min. The removal depths, estimated from weight-loss measurements, were $\Delta t = 3.90$ μm and 4.01 μm for A1 and B1, respectively. The measured internal quality factors at $T < 20$ mK were relatively low: $Q_{\text{int}} = 4.55 \times 10^8$ for A1 and 6.63×10^8 for B1 (Table I).

In the second trial, a wBCP solution with a 1 : 1 : 2 volume ratio was prepared. This time, the container holding the solution was immersed in ice water, and the solution temperature was maintained at 5 °C. Taking into account the exponentially slower reaction rate at this low temperature, a wBCP flush was applied to cavity A1 for 15 min, followed by rinsing and ultrasonic cleaning in ultrapure water for 15 min. The removal depth, estimated from the weight-loss measurement, was $\Delta t = 15$ μm. The measured internal quality factor at $T < 20$ mK was $Q_{\text{int}} = 1.15 \times 10^9$, which was better than that obtained in the first wBCP trial but was only comparable to the values achieved with the standard BCP flush using H_3PO_4 as the buffering component. For example, the B1 and B2 cavities treated with the standard BCP flush at room temperature exhibited internal quality factors of $Q_{\text{int}} = 8.71 \times 10^8$ and 1.14×10^9, respectively, measured at base temperature $T < 20$ mK (Table I). We did not observe any clear indication that low-temperature wBCP provides superior performance compared to the room-temperature standard BCP process.

APPENDIX D: SAMPLE PREPARATION AND MEASUREMENT SETUP

After surface treatments, the cavities were stored in air for several days to stabilize the growth of native niobium oxides. Only cavity B2, after 600 °C mid-temperature annealing, was sealed in vacuum immediately after removal from the vacuum furnace and opened 30 min before installation into the experimental setup. All cavities underwent multiple cooldown cycles; after warming back to room temperature, they were exposed to air

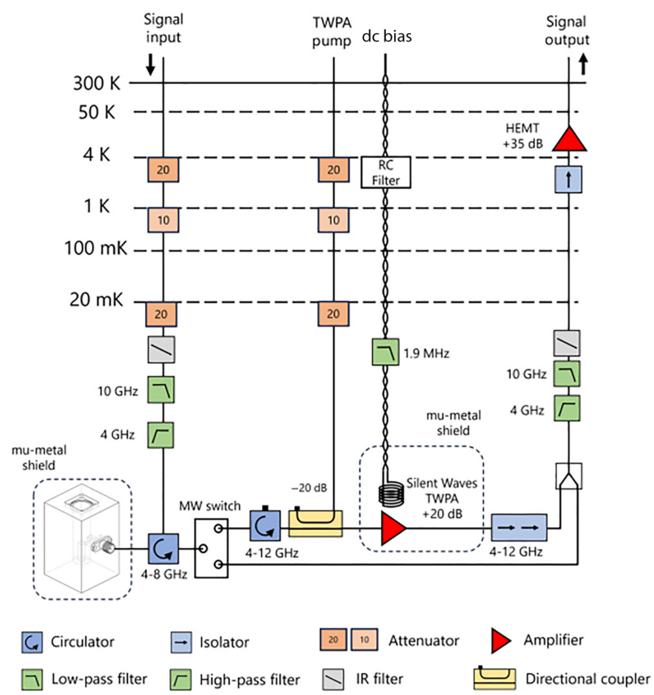

FIG. 6. Cryogenic measurement setup employed in the experiment. The reflected signal from the sample is routed by a cryogenic rf switch. For low-power measurements, the signal is amplified by 20 dB with a TWPA from Silent Waves (The Carthago). The signal is further amplified by 35 dB with a high-electron-mobility transistor (HEMT) amplifier from LNF.

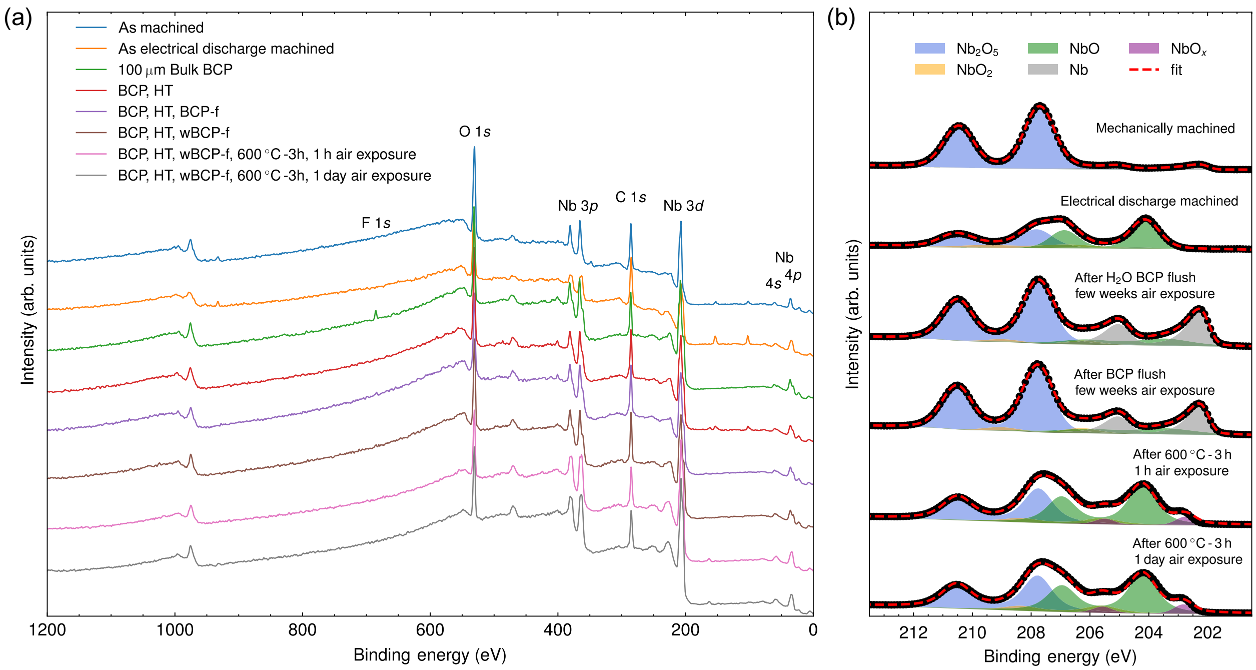

FIG. 7. (a) Evolution of XPS spectrum before and after various surface treatments. (b) XPS spectrum of Nb 3*d* region for as-machined sample and after each procedure (bold black line). Peaks are fitted by considering Nb_2O_5, NbO_2, NbO, NbO_x ($0 < x < 1$), and metallic Nb, and they are indicated with filled areas of various colors; the sum of all fitted peaks is then shown as the dashed red line.

for several hours during the process of exchanging other samples mounted on the dilution refrigerator.

The external quality factor Q_{ext} of the cavity is controlled by adjusting the insertion depth of the SMA connector's center pin, which couples to the cavity for reflection measurements. The value of Q_{ext} is set to a slightly overcoupled condition ($Q_{\mathrm{ext}} \leq Q_{\mathrm{int}}$), which enables measurements in the quasiparticle-dominant regime $T \geq 1.5$ K with high signal-to-noise ratio, where Q_{int} is expected to decrease. In contrast, the 600 °C-annealed cavity B2 is measured under both undercoupled ($Q_{\mathrm{ext}} > Q_{\mathrm{int}}$) and slightly overcoupled conditions. This is because, under overcoupled conditions, the total cavity decay time τ_{tot} is dominated by the external decay time τ_{ext}, making it difficult to observe the intrinsic long-lived nature of the high-Q cavity in the time domain.

The top cap of a high-Q coaxial cavity is typically sealed with indium. In this work, however, measurements were performed either without a cap or with a cap secured only by screws. This is because the electromagnetic field of the $\lambda/4$ mode decays to insignificance at the cap position, as the distance from the tip of the center stub is approximately 25 mm. Experimentally, no significant difference in Q_{int} was observed with or without the cap. Nonetheless, indium sealing may still provide a further improvement in Q_{int}.

The detailed cryogenic setup is shown in Fig. 6. An rf switch (Radiall R577433002) is installed after the circulator, enabling measurement of the reflection coefficient S_{11} of the cavity under both high-power and low-power signals. For low-power signal measurements, the signal is amplified with a TWPA (Silent Waves, The Carthago). The TWPA requires a dc magnetic flux for optimal performance, and the dc current for the local magnet (mounted inside the TWPA package) is supplied by an ADCMT 6166 high-precision dc voltage-current source. An Agilent E8267C is used to generate the rf pump signal for the TWPA. Frequency-domain measurements were performed by an Agilent N5232A PNA-L network analyzer.

APPENDIX E: XPS MEASUREMENTS

To identify the niobium oxides and other residues present on the cavity surface after each treatment step, we performed XPS measurements and analysis for reference samples. The XPS measurements were carried out using an XPS5700 (PHI) at 45° with a monochromatic Al–Kα source (1486.6 eV). The spectra were fitted using LG4X-V2 [70]. For peak fitting, an asymmetric line shape was employed for metallic niobium, while a symmetric Gaussian-Lorentzian line shape was used for niobium oxides. An area constraint of 3 : 2 was applied to the spin-orbit doublets of Nb $3d_{3/2}$ and Nb $3d_{5/2}$ levels, and the binding-energy separation between them was fixed at 2.75 eV. It is assumed that Nb_2O_5 forms on the outermost

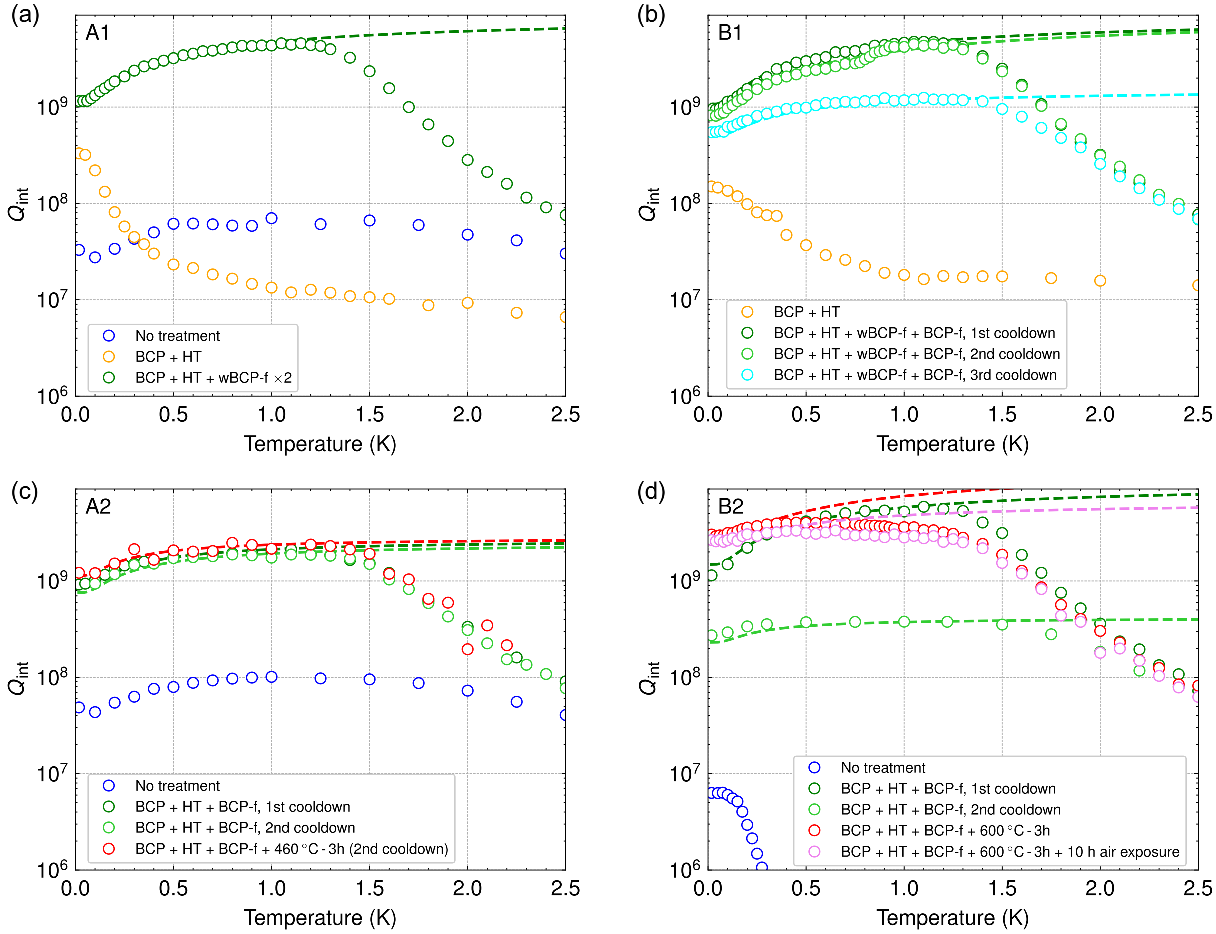

FIG. 8. Temperature dependence of $Q_{\rm int}$ for all measured cavities: (a) A1, (b) B1, (c) A2, and (d) B2. Definitions: BCP, 100-μm BCP; HT, 900 °C–3 h; BCP-f, BCP flush with standard BCP mixture; wBCP-f, water-buffered BCP flush. The dashed lines are fits to $Q_{\rm int}(T)$ using the temperature-dependent TLS model [Eq. (2)]. These measurements were performed at an average photon number of $\bar{n} \sim 10^4$.

surface of all samples; therefore, its binding energy was used for peak alignment [42,48,49].

Figure 7(a) shows the survey spectrum of the reference niobium sample after each treatment procedure. The surface after the initial approximately 100-μm bulk BCP shows a clear signature of F 1*s* around 685 eV, implying the presence of fluorine bound to niobium [31,71]. Figure 7(b) displays the corresponding XPS spectra of the Nb 3*d* region. The spectrum for the as-machined sample (top) shows prominent peaks originating from Nb_2O_5, and this is commonly observed on untreated niobium surfaces. In contrast, the spectrum for the EDM-finished sample is completely different. As mentioned in the main text, an EDM-finished cavity exhibits an order-of-magnitude smaller $Q_{\rm int}$ than cavities fabricated by machining alone, and its temperature dependence differs significantly (blue symbols in Fig. 8). This behavior most likely originates from the EDM-induced formation of a low-T_c material on the cavity surface. It is widely known that EDM forms a recast layer tens of micrometers thick at the surface, which contains carbon and hydrogen contamination from insulating oil used in EDM. This is consistent with the absence of metallic-Nb-related peaks in the EDM-finished sample.

After 900 °C baking following BCP flush, the Nb_2O_5 ratio decreases compared to the untreated niobium sample surface. The composition ratio of Nb_2O_5, estimated from the peak area of the XPS spectrum, decreases from 87.8% to 57.5% after a water-buffered BCP flush (wBCP-f) and to 61.0% after a conventional BCP flush (BCP-f). Annealing at 600 °C further reduces the Nb_2O_5 ratio to 40.8%. Meanwhile, the NbO ratio increases from 0.83% (as-machined) to 12.3% (wBCP-f) and 11.9% (BCP-f) after 900 °C baking, eventually reaching 43.7% after 600 °C annealing.

It should be noted that metallic-Nb peaks around 202 eV become undetectable after 600 °C annealing, suggesting the presence of a thick NbO layer just beneath the

TABLE I. Summary of the internal quality factors Q_{int}, internal lifetimes, residual resistances, and loss tangents of 3D coaxial cavities with various surface treatments. Definitions: BCP, 100-μm BCP; HT, 900 °C–3 h high-temperature baking; BCP-f, BCP flush with standard BCP mixture; wBCP-f, water-buffered BCP flush. The parameters for TLS fitting ($F\delta^0_{TLS}$ and Q_{res}) are extracted from the average photon-number dependence of Q_{int} at base temperature $T < 20$ mK.

			$T < 20$ mK			$T = 1.2$ K		TLS fit	
Cavity	Treatment	Cooldown cycles	Q_{int} ($\times 10^6$)	R_s (nΩ)	τ_{int} (ms)	Q_{int} ($\times 10^6$)	R_s (nΩ)	$F\delta^0_{TLS}$	Q_{res}
A1	No treatment		32.9	2000	0.969	60.9	1080	1.43×10^{-8}	4.23×10^7
	BCP + HT	1	358	185	10.5	12.3	5410	1.15×10^{-9}	5.33×10^8
		2	331	200	9.67	12.7	5210	1.85×10^{-10}	3.49×10^8
	BCP + HT + wBCP-f		455	146	13.3	–	–	2.93×10^{-10}	5.26×10^9
	BCP + HT + wBCP-f × 2		1150	57.6	33.5	4590	14.5	6.39×10^{-10}	3.05×10^9
B1	BCP + HT		150	441	4.4	17.6	3750	–	–
	BCP + HT + wBCP-f		663	98	19.4	–	–	9.68×10^{-10}	1.81×10^9
	BCP + HT + wBCP-f + BCP-f	1	871	76.0	25.4	4590	14.4	9.93×10^{-10}	6.50×10^9
		2	828	80.0	24.2	4110	16.1	1.06×10^{-9}	5.27×10^9
		3	538	123	15.7	1190	55.5	1.19×10^{-9}	1.46×10^9
A2	No treatment		48.7	1350	1.43	97.4	674	4.31×10^{-10}	4.98×10^7
	BCP + HT + BCP-f	1	917	72.3	26.7	1890	35.0	9.62×10^{-10}	4.92×10^9
		2	784	84.5	22.9	1870	35.3	1.22×10^{-9}	4.60×10^9
	BCP + HT + BCP-f + 460 °C–3 h	1	1220	54.3	35.6	–	–	4.85×10^{-10}	2.90×10^9
		2	1180	56.0	34.5	2390	27.8	4.98×10^{-10}	3.22×10^9
		3	1250	52.9	36.6	–	–	4.67×10^{-10}	2.86×10^9
		4	1240	53.6	36.0	–	–	4.90×10^{-10}	2.80×10^9
B2	No treatment		6.31	10 400	0.185	–	–	1.32×10^{-8}	6.84×10^6
	BCP + HT + BCP-f	1	1140	58.0	33.3	5570	11.9	6.13×10^{-9}	3.56×10^9
		2	286	232	8.32	377	10.9	1.61×10^{-9}	5.08×10^8
	BCP + HT + BCP-f + 600 °C–3 h	1	3030	21.9	88.3	3190	20.8	2.10×10^{-10}	7.41×10^9
		2	2640	25.1	77.0	26.1	74.2	1.82×10^{-10}	4.77×10^9

outermost Nb_2O_5 layer. This likely helps to suppress the regrowth of Nb_2O_5 upon air exposure, and these observations are consistent with an earlier report by Yu *et al.* [48].

APPENDIX F: CAVITY PERFORMANCE DETAILS

The temperature dependence of Q_{int} for all cavities measured in this work is shown in Fig. 8, and the extracted parameters are listed in Table I.

[1] Hanhee Paik, D. I. Schuster, Lev S. Bishop, G. Kirchmair, G. Catelani, A. P. Sears, B. R. Johnson, M. J. Reagor, L. Frunzio, L. I. Glazman, S. M. Girvin, M. H. Devoret, and R. J. Schoelkopf, Observation of high coherence in Josephson junction qubits measured in a three-dimensional circuit QED architecture, Phys. Rev. Lett. **107**, 240501 (2011).

[2] Matthew Reagor, Wolfgang Pfaff, Christopher Axline, Reinier W. Heeres, Nissim Ofek, Katrina Sliwa, Eric Holland, Chen Wang, Jacob Blumoff, Kevin Chou, Michael J. Hatridge, Luigi Frunzio, Michel H. Devoret, Liang Jiang, and Robert J. Schoelkopf, Quantum memory with millisecond coherence in circuit QED, Phys. Rev. B **94**, 014506 (2016).

[3] Nissim Ofek, Andrei Petrenko, Reinier Heeres, Philip Reinhold, Zaki Leghtas, Brian Vlastakis, Yehan Liu, Luigi Frunzio, Steven M. Girvin, Liang Jiang, *et al.*, Extending the lifetime of a quantum bit with error correction in superconducting circuits, Nature **536**, 441 (2016).

[4] Yvonne Y. Gao, Brian J. Lester, Kevin S. Chou, Luigi Frunzio, Michel H. Devoret, Liang Jiang, S. M. Girvin, and Robert J. Schoelkopf, Entanglement of Bosonic modes through an engineered exchange interaction, Nature **566**, 509 (2019).

[5] Volodymyr V. Sivak, Alec Eickbusch, Baptiste Royer, Shraddha Singh, Ioannis Tsioutsios, Suhas Ganjam, Alessandro Miano, B. L. Brock, A. Z. Ding, Luigi Frunzio, *et al.*, Real-time quantum error correction beyond break-even, Nature **616**, 50 (2023).

[6] Zhongchu Ni, Sai Li, Xiaowei Deng, Yanyan Cai, Libo Zhang, Weiting Wang, Zhen-Biao Yang, Haifeng Yu, Fei Yan, Song Liu, *et al.*, Beating the break-even point with a discrete-variable-encoded logical qubit, Nature **616**, 56 (2023).

[7] Mattia Checchin, Daniil Frolov, Andrei Lunin, Anna Grassellino, and Alexander Romanenko, Measurement of the low-temperature loss tangent of high-resistivity silicon using a high-Q superconducting resonator, Phys. Rev. Appl. **18**, 034013 (2022).

[8] Alexander P. Read, Benjamin J. Chapman, Chan U. Lei, Jacob C. Curtis, Suhas Ganjam, Lev Krayzman, Luigi

Frunzio, and Robert J. Schoelkopf, Precision measurement of the microwave dielectric loss of sapphire in the quantum regime with parts-per-billion sensitivity, Phys. Rev. Appl. **19**, 034064 (2023).

[9] A. Romanenko, R. Harnik, A. Grassellino, R. Pilipenko, Y. Pischalnikov, Z. Liu, O. S. Melnychuk, B. Giaccone, O. Pronitchev, T. Khabiboulline, *et al.*, Search for dark photons with superconducting radio frequency cavities, Phys. Rev. Lett. **130**, 261801 (2023).

[10] Ankur Agrawal, Akash V. Dixit, Tanay Roy, Srivatsan Chakram, Kevin He, Ravi K. Naik, David I. Schuster, and Aaron Chou, Stimulated emission of signal photons from dark matter waves, Phys. Rev. Lett. **132**, 140801 (2024).

[11] K. Nakazono, S. Chen, H. Fukuda, Y. Iiyama, T. Inada, T. Moroi, T. Nitta, A. Noguchi, R. Sawada, S. Shirai, *et al.*, Search for dark photon dark matter of a mass around 36.1 μeV using a frequency-tunable cavity controlled through a coupled superconducting qubit, arXiv:2505.15619.

[12] M. Kudra, J. Biznárová, A. Fadavi Roudsari, J. J. Burnett, D. Niepce, S. Gasparinetti, B. Wickman, and P. Delsing, High quality three-dimensional aluminum microwave cavities, Appl. Phys. Lett. **117**, 070601 (2020).

[13] T. Kubo, Y. Ajima, H. Inoue, K. Umemori, Y. Watanabe, and M. Yamanaka, in *Proc. 5th International Particle Accelerator Conference (IPAC'14), Dresden, Germany, June 15–20, 2014*, Vol. 5 in International Particle Accelerator Conference (JACoW, Geneva, Switzerland, 2014), pp. 2519–2521. https://doi.org/10.18429/JACoW-IPAC2014-WEPRI022.

[14] A. Romanenko and D. I. Schuster, Understanding quality factor degradation in superconducting niobium cavities at low microwave field amplitudes, Phys. Rev. Lett. **119**, 264801 (2017).

[15] A. Romanenko, R. Pilipenko, S. Zorzetti, D. Frolov, M. Awida, S. Belomestnykh, S. Posen, and A. Grassellino, Three-dimensional superconducting resonators at $T < 20$ mK with photon lifetimes up to $\tau = 2$ s, Phys. Rev. Appl. **13**, 034032 (2020).

[16] Mark K. Transtrum, Gianluigi Catelani, and James P. Sethna, Superheating field of superconductors within Ginzburg-Landau theory, Phys. Rev. B **83**, 094505 (2011).

[17] F. Pei, J. Lin, and A. Gurevich, Effect of impurities on the superheating field of type-II superconductors, Phys. Rev. B **85**, 054513 (2012).

[18] Takayuki Kubo, Superfluid flow in disordered superconductors with Dynes pair-breaking scattering: Depairing current, kinetic inductance, and superheating field, Phys. Rev. Res. **2**, 033203 (2020).

[19] Hasan Padamsee, 50 years of success for SRF accelerators—a review, Supercond. Sci. Technol. **30**, 053003 (2017).

[20] Bianca Giaccone, Martina Martinello, Paolo Berrutti, Oleksandr Melnychuk, Dmitri A. Sergatskov, Anna Grassellino, Dan Gonnella, Marc Ross, Marc Doleans, and John F. Zasadzinski, Field emission mitigation studies in the SLAC Linac Coherent Light Source II superconducting rf cavities via in situ plasma processing, Phys. Rev. Accel. Beams **24**, 022002 (2021).

[21] Hiroshi Sakai, Enrico Cenni, Kazuhiro Enami, Takaaki Furuya, Masaru Sawamura, Kenji Shinoe, and Kensei Umemori, Field emission studies in vertical test and during cryomodule operation using precise x-ray mapping system, Phys. Rev. Accel. Beams **22**, 022002 (2019).

[22] Zuhawn Sung, Arely Cano, Akshay Murthy, Daniel Bafia, Evguenia Karapetrova, Martina Martinello, Jaeyel Lee, Anna Grassellino, and Alexander Romanenko, Direct observation of nanometer size hydride precipitations in superconducting niobium, Sci. Rep. **14**, 26916 (2024).

[23] J. M. Cavedon, M. Juillard, A. Godin, C. Henriot, P. Leconte, H. Safa, A. Veyssiere, B. Aune, B. Bonin, and C. Zylberajch, in *Proc. the Linear Accelerator Conference 1990, Albuquerque, New Mexico, USA, 1990* (JACoW, Geneva, Switzerland, 1990), p. 253.

[24] K. Saito and P. Kneisel, in *Proc. the Third European Particle Accelerator Conference, Berlin, Germany, 1992* (JACoW, Geneva, Switzerland, 1992), p. 1231.

[25] Yoshihisa Iwashita, Yujiro Tajima, and Hitoshi Hayano, Development of high resolution camera for observations of superconducting cavities, Phys. Rev. ST Accel. Beams **11**, 093501 (2008).

[26] M. Ge, G. Wu, D. Burk, J. Ozelis, E. Harms, D. Sergatskov, D. Hicks, and L. D. Cooley, Routine characterization of 3D profiles of SRF cavity defects using replica techniques, Supercond. Sci. Technol. **24**, 035002 (2011).

[27] A. Romanenko, A. Grassellino, A. C. Crawford, D. A. Sergatskov, and O. S. Melnychuk, Ultra-high quality factors in superconducting niobium cavities in ambient magnetic fields up to 190 mG, Appl. Phys. Lett. **105**, 234103 (2014).

[28] Shichun Huang, Takayuki Kubo, and R. L. Geng, Dependence of trapped-flux-induced surface resistance of a large-grain Nb superconducting radio-frequency cavity on spatial temperature gradient during cooldown through T_c, Phys. Rev. Accel. Beams **19**, 082001 (2016).

[29] Ofir Milul, Barkay Guttel, Uri Goldblatt, Sergey Hazanov, Lalit M. Joshi, Daniel Chausovsky, Nitzan Kahn, Engin Çiftyürek, Fabien Lafont, and Serge Rosenblum, Superconducting cavity qubit with tens of milliseconds single-photon coherence time, PRX Quantum **4**, 030336 (2023).

[30] Taeyoon Kim *et al.*, Ultracoherent superconducting cavity-based multiqudit platform with error-resilient control, arXiv:2506.03286.

[31] Andrew E. Oriani, Fang Zhao, Tanay Roy, Alexander Anferov, Kevin He, Ankur Agrawal, Riju Banerjee, Srivatsan Chakram, and David I. Schuster, Niobium coaxial cavities with internal quality factors exceeding 1.4×10^9 for circuit quantum electrodynamics, Phys. Rev. Appl. **24**, 044080 (2025).

[32] S. Posen, A. Romanenko, A. Grassellino, O. S. Melnychuk, and D. A. Sergatskov, Ultralow surface resistance via vacuum heat treatment of superconducting radio-frequency cavities, Phys. Rev. Appl. **13**, 014024 (2020).

[33] H. Ito, H. Araki, K. Takahashi, and K. Umemori, Influence of furnace baking on Q–E behavior of superconducting accelerating cavities, Prog. Theor. Exp. Phys. **2021**, 071G01 (2021).

[34] H. Inoue, T. Kubo, T. Saeki, Y. Watanabe, S. Yamaguchi, M. Yamanaka, and Y. Ajima, in *Proceedings of SRF2013,*

Paris, France, 2013, Vol. 16 in International Conference on RF Superconductivity (JACoW, Geneva, Switzerland, 2013), pp. 821–824.

[35] Y. Kalboussi, I. Curci, F. Miserque, D. Troadec, N. Brun, M. Walls, G. Jullien, F. Eozenou, M. Baudrier, L. Maurice, Q. Bertrand, P. Sahuquet, and T. Proslier, Crystallinity in niobium oxides: A pathway to mitigate two-level-system defects in niobium three-dimensional resonators for quantum applications, Phys. Rev. Appl. **23**, 044023 (2025).

[36] S. Probst, F. B. Song, P. A. Bushev, A. V. Ustinov, and M. Weides, Efficient and robust analysis of complex scattering data under noise in microwave resonators, Rev. Sci. Instrum. **86**, 024706 (2015).

[37] Jiansong Gao, Miguel Daal, Anastasios Vayonakis, Shwetank Kumar, Jonas Zmuidzinas, Bernard Sadoulet, Benjamin A. Mazin, Peter K. Day, and Henry G. Leduc, Experimental evidence for a surface distribution of two-level systems in superconducting lithographed microwave resonators, Appl. Phys. Lett. **15**, 152505 (2008).

[38] H. Wang, M. Hofheinz, J. Wenner, M. Ansmann, R. C. Bialczak, M. Lenander, Erik Lucero, M. Neeley, A. D. O'Connell, D. Sank, M. Weides, A. N. Cleland, and John M. Martinis, Improving the coherence time of superconducting coplanar resonators, Appl. Phys. Lett. **95**, 233508 (2009).

[39] Clemens Müller, Jared H. Cole, and Jürgen Lisenfeld, Towards understanding two-level-systems in amorphous solids: Insights from quantum circuits, Rep. Prog. Phys. **82**, 124501 (2019).

[40] C. R. H. McRae, H. Wang, J. Gao, M. R. Vissers, T. Brecht, A. Dunsworth, D. P. Pappas, and J. Mutus, Materials loss measurements using superconducting microwave resonators, Rev. Sci. Instrum. **91**, 091101 (2020).

[41] Chan U. Lei, Lev Krayzman, Suhas Ganjam, Luigi Frunzio, and Robert J. Schoelkopf, High coherence superconducting microwave cavities with indium bump bonding, Appl. Phys. Lett. **116**, 154002 (2020).

[42] M. V. P. Altoé, A. Banerjee, C. Berk, A. Hajr, A. Schwartzberg, C. Song, M. Alghadeer, S. Aloni, M. J. Elowson, J. M. Kreikebaum, E. K. Wong, S. M. Griffin, S. Rao, A. Weber-Bargioni, A. M. Minor, D. I. Santiago, S. Cabrini, I. Siddiqi, and D. F. Ogletree, Localization and mitigation of loss in niobium superconducting circuits, PRX Quantum **3**, 020312 (2022).

[43] Alex Gurevich and Takayuki Kubo, Surface impedance and optimum surface resistance of a superconductor with an imperfect surface, Phys. Rev. B **96**, 184515 (2017).

[44] Takayuki Kubo, Effects of nonmagnetic impurities and subgap states on the kinetic inductance, complex conductivity, quality factor, and depairing current density, Phys. Rev. Appl. **17**, 014018 (2022).

[45] Paul Heidler, Christian M. F. Schneider, Katja Kustura, Carlos Gonzalez-Ballestero, Oriol Romero-Isart, and Gerhard Kirchmair, Non-Markovian effects of two-level systems in a niobium coaxial resonator with a single-photon lifetime of 10 milliseconds, Phys. Rev. Appl. **16**, 034024 (2021).

[46] Y. Kalboussi, B. Delatte, S. Bira, K. Dembele, X. Li, F. Miserque, N. Brun, M. Walls, J. L. Maurice, D. Dragoe, J. Leroy, D. Longuevergne, A. Gentils, S. Jublot-Leclerc, G. Jullien, F. Eozenou, M. Baudrier, L. Maurice, and T. Proslier, Reducing two-level systems dissipations in 3D superconducting niobium resonators by atomic layer deposition and high temperature heat treatment, Appl. Phys. Lett. **124**, 134001 (2024).

[47] D. Bafia, A. Murthy, A. Grassellino, and A. Romanenko, Oxygen vacancies in niobium pentoxide as a source of two-level system losses in superconducting niobium, Phys. Rev. Appl. **22**, 024035 (2024).

[48] Mingming Yu, Guo Pu, Yi Xue, Sishu Wang, Sheng Chen, Yihan Wang, Li Yang, Zhijun Wang, Tongtong Zhu, Teng Tan, Yuan He, Shichun Huang, and Kun Zhang, The oxidation behaviors of high-purity niobium for superconducting radio-frequency cavity application in vacuum heat treatment, Vacuum **203**, 111258 (2022).

[49] J. Verjauw, A. Potočnik, M. Mongillo, R. Acharya, F. Mohiyaddin, G. Simion, A. Pacco, T. Ivanov, D. Wan, A. Vanleenhove, L. Souriau, J. Jussot, A. Thiam, J. Swerts, X. Piao, S. Couet, M. Heyns, B. Govoreanu, and I. Radu, Investigation of microwave loss induced by oxide regrowth in high-Q niobium resonators, Phys. Rev. Appl. **16**, 014018 (2021).

[50] N. Pupeter, E. Mahner, P. Kneisel, and G. Muller, in *Proc. the Sixth Workshop on RF Superconductivity, CEBAF, Newport News, Virginia, USA, 1993* (JACoW, Geneva, Switzerland, 1993), p. 1085.

[51] T. Furuya, S. Mitsunobu, S. Noguchi, K. Hosoyama, T. Nakazato, T. Tajima, K. Asano, K. Inoue, Y. Iino, H. Nomura, K. Saito, Y. Kojima, and K. Takeuchi, in *Proc. the Fourth Workshop on RF Superconductivity, KEK, Tsukuba, Japan, 1989* (JACoW, Geneva, Switzerland, 1989), p. 635.

[52] B. Piosczyk, P. Kneisel, O. Stoltz, and J. Halbritter, Investigations of additional losses in superconducting niobium cavities due to frozen-in flux, IEEE Trans. Nucl. Sci. **20**, 108 (1973).

[53] S. Posen, M. Checchin, A. C. Crawford, A. Grassellino, M. Martinello, O. S. Melnychuk, A. Romanenko, D. A. Sergatskov, and Y. Trenikhina, Efficient expulsion of magnetic flux in superconducting radiofrequency cavities for high Q applications, J. Appl. Phys. **119**, 213903 (2016).

[54] S. Ooi, M. Tachiki, T. Konomi, T. Kubo, A. Kikuchi, S. Arisawa, H. Ito, and K. Umemori, Observation of intermediate mixed state in high-purity cavity-grade Nb by magneto-optical imaging, Phys. Rev. B **104**, 064504 (2021).

[55] S. Ooi, M. Tachiki, T. Mochiku, H. Ito, T. Kubo, A. Kikuchi, S. Arisawa, and K. Umemori, Dynamical visualization of attractively interacting single vortices in type-II/1 superconducting Nb by magneto-optical imaging, Phys. Rev. B **111**, 094519 (2025).

[56] T. Konomi *et al.*, in *Proc. of International Conference on RF Superconductivity (SRF'17), Lanzhou, China, July 17–21, 2017*, Vol. 18 in International Conference on RF Superconductivity (JACoW, Geneva, Switzerland, 2018), pp. 775–778. https://doi.org/10.18429/JACoW-SRF2017-THPB021.

[57] Marc Wenskat, Christopher Bate, Arti Dangwal Pandey, Arno Jeromin, Thomas F. Keller, Jens Knobloch, Julia Köszegi, Felix Kramer, Oliver Kugeler, Satish Kulkarni, Detlef Reschke, Jörn Schaffran, Guilherme Dalla Lana Semione, Sven Sievers, Lea Steder, Andreas Stierle, and

Nicholas Walker, Nitrogen infusion R&D at DESY a case study on cavity cut-outs, Supercond. Sci. Technol. **33**, 115017 (2020).

[58] W. Singer, A. Brinkmann, R. Brinkmann, J. Iversen, A. Matheisen, W.-D. Moeller, A. Navitski, D. Reschke, J. Schaffran, A. Sulimov, N. Walker, H. Weise, P. Michelato, L. Monaco, C. Pagani, and M. Wiencek, Production of superconducting 1.3-GHz cavities for the European X-ray Free Electron Laser, Phys. Rev. Accel. Beams **19**, 092001 (2016).

[59] K. Twarowski, P. Schmuser, D. Bloess, E. Haebel, E. Chiaveri, J.-M. Tessier, H. Preis, H. Wenninger, H. Safa, L. Lilje, D. Reschke, and J.-P. Charrier, in *Proc. the Nineth Workshop on RF Superconductivity, La Fonda Hotel, Santa Fe, New Mexico, USA, 1999* (JACoW, Geneva, Switzerland, 1999), p. 74.

[60] D. Bafia, A. Grassellino, O. S. Melnychuk, A. S. Romanenko, Z.-H. Sung, and J. Zasadzinski, in *Proc. SRF'19*, Vol. 19 in International Conference on RF Superconductivity (JACoW Publishing, Geneva, Switzerland, 2019), pp. 586–591. https://doi.org/10.18429/JACoW-SRF2019-TUP061.

[61] Gianluigi Ciovati, Improved oxygen diffusion model to explain the effect of low-temperature baking on high field losses in niobium superconducting cavities, Appl. Phys. Lett. **89**, 022507 (2006).

[62] E. M. Lechner, J. W. Angle, A. D. Palczewski, F. A. Stevie, M. J. Kelley, and C. E. Reece, Oxide dissolution and oxygen diffusion scenarios in niobium and implications on the Bean–Livingston barrier in superconducting cavities, J. Appl. Phys. **135**, 133902 (2024).

[63] Takayuki Kubo, Multilayer coating for higher accelerating fields in superconducting radio-frequency cavities: A review of theoretical aspects, Supercond. Sci. Technol. **30**, 023001 (2017).

[64] Vudtiwat Ngampruetikorn and J. A. Sauls, Effect of inhomogeneous surface disorder on the superheating field of superconducting RF cavities, Phys. Rev. Res. **1**, 012015(R) (2019).

[65] Takayuki Kubo, Superheating fields of semi-infinite superconductors and layered superconductors in the diffusive limit: Structural optimization based on the microscopic theory, Supercond. Sci. Technol. **34**, 045006 (2021).

[66] P. Sha, W. M. Pan, S. Jin, J. Y. Zhai, Z. H. Mi, B. Q. Liu, C. Dong, F. S. He, R. Ge, L. R. Sun, and S. A. Zheng, Ultrahigh accelerating gradient and quality factor of CEPC 650 MHz superconducting radio-frequency cavity, Nucl. Sci. Tech. **33**, 125 (2022).

[67] Takayuki Kubo and Alex Gurevich, Field-dependent nonlinear surface resistance and its optimization by surface nanostructuring in superconductors, Phys. Rev. B **100**, 064522 (2019).

[68] W. Hartung, C. Hauviller, W. Weingarten, P. Bosland, P. Bernard, D. Bloess, and J. M. Martignac, in *Proc. the Fifth Workshop on RF Superconductivity, DESY, Hamburg, Germany, 1991* (JACoW, Geneva, Switzerland, 1991), p. 487.

[69] K. Kurosawa, P. Kneisel, S. Noguchi, E. Kako, M. Ono, T. Shishido, K. Saito, H. Miwa, and T. Suzuki, in *Proc. the Sixth Workshop on RF Superconductivity, CEBAF, Newport News, Virginia, USA, 1993* (JACoW, Geneva, Switzerland, 1993), p. 1151.

[70] Julian Andreas Hochhaus and Hideki Nakajima, LG4X-V2 (2.3.1), https://doi.org/10.5281/zenodo.7777422

[71] Alena Prudnikava, Yegor Tamashevich, Anna Makarova, Dmitry Smirnov, and Jens Knobloch, In-situ synchrotron x-ray photoelectron spectroscopy study of medium-temperature baking of niobium for SRF application, Supercond. Sci. Technol. **37**, 075007 (2024).